Structure, Vol. 10, 1159–1171, September, 2002, ©2002 Elsevier Science Ltd. All rights reserved. PII S0969-2126(02)00796-7

Betaine-Homocysteine Methyltransferase: Zinc in a Distorted Barrel

John C. Evans,[1] Donald P. Huddler,[1] Jiri Jiracek,[2] Carmen Castro,[3] Norman S. Millian,[3] Timothy A. Garrow,[3] and Martha L. Ludwig[1,4]
[1]Biophysics Research Division and
Department of Biological Chemistry
University of Michigan, Ann Arbor
Ann Arbor, Michigan 48109
[2]Department of Peptide Biochemistry
Institute of Organic Chemistry and Biochemistry
Academy of Sciences of the Czech Republic
Flemingovo nam. 2
166 10 Prague 6
Czech Republic
[3]Department of Food Science and Human Nutrition
University of Illinois, Urbana
Urbana, Illinois 61801

Summary

Betaine-homocysteine methyl transferase (BHMT) catalyzes the synthesis of methionine from betaine and homocysteine (Hcy), utilizing a zinc ion to activate Hcy. BHMT is a key liver enzyme that is important for homocysteine homeostasis. X-ray structures of human BHMT in its oxidized (Zn-free) and reduced (Zn-replete) forms, the latter in complex with the bisubstrate analog, S(δ-carboxybutyl)-L-homocysteine, were determined at resolutions of 2.15 Å and 2.05 Å. BHMT is a $(\beta/\alpha)_8$ barrel that is distorted to construct the substrate and metal binding sites. The zinc binding sequences G-V/L-N-C and G-G-C-C are at the C termini of strands β6 and β8. Oxidation to the Cys217-Cys299 disulfide and expulsion of Zn are accompanied by local rearrangements. The structures identify Hcy binding fingerprints and provide a prototype for the homocysteine S-methyltransferase family.

Introduction

Betaine-homocysteine methyltransferase (BHMT; EC 2.1.1.5) and methionine synthase (MetH) are the two enzymes that convert homocysteine to methionine in mammals, thereby exerting important effects on the cellular and plasma levels of homocysteine (Hcy). BHMT is more restricted than MetH in its tissue distribution; it is found in kidney and liver and, according to model studies [1], can account for approximately half of the methionine synthesized in the liver. Hcy pools are depleted by the reactions catalyzed by MetH, BHMT, and cystathionine β-synthase and are in turn replenished by hydrolysis of S-adenosylhomocysteine [1, 2]. Metabolic fluxes in the pathways that lead to and from Hcy have long attracted interest because of the inborn errors that occur in enzymes in these pathways [3]. Within the last decade, elevated homocysteine has been widely recognized as an important independent risk factor for development of cardiovascular disease [4–6], and, very recently, it has been suggested to play a role in the etiology of Alzheimer's disease [7, 8].

BHMT catalyzes the transfer of a methyl group from glycine betaine to homocysteine, forming methionine and dimethylglycine (Figure 1A). It also utilizes the sulfonium analog, dimethylacetothetin (dimethylthioacetate), as a methyl donor and has been purified as a thetin-homocysteine methyltransferase [9, 10]. The enzymes from horse, pig, and rat liver were isolated and characterized by several groups, starting in the 1950s [9, 11, 12]; *H. sapiens* BHMT was first purified by Skiba et al. [13] and has been cloned and expressed by Garrow and coworkers [14–16]. BHMT is an oligomeric protein, most frequently reported to be a hexamer of ~45 kDa units [9, 13, 17]. From steady-state kinetic analyses, Fromm and Nordlie [12] concluded that the reaction involves a ternary complex; inhibition patterns are consistent with an ordered reaction [18]. A bisubstrate inhibitor designed to mimic the transition state for methyl transfer, S(δ-carboxybutyl)-L-homocysteine [19], binds with μM affinity (Figure 1B).

The discovery that zinc ion is essential for the alkylation of thiols catalyzed by BHMT, MetH, and related subfamilies of methyltransferases is relatively recent [20]. The first clues came from the mutation of conserved cysteine residues, in particular, the vicinal Cys-Cys embedded in the Gly-Gly-Cys-Cys sequences of BHMT [14–16] and B_{12}-dependent methionine synthase [20, 21]. Depletion of zinc and loss of activity in these mutants, as well as zinc removal and reconstitution in the wild-type enzymes, established an essential role for the metal ion [16, 22]. In retrospect it seems surprising that the requirement for zinc was not recognized earlier, but modest concentrations of EDTA do not readily extract the Zn^{2+} from these proteins. In MetH, binding of Hcy at a neutral pH is accompanied by deprotonation, consistent with ligation of the thiolate anion of Hcy to the essential zinc [22]. EXAFS spectroscopy has established that homocysteine and selenohomocysteine are bound to the zinc [23, 24].

Evidence is emerging that some of the zinc-dependent enzymes activating alkyl transfer to thiols are prone to oxidative inactivation and loss of zinc. Inactivation has been assumed to involve formation of a disulfide incorporating at least one of the cysteine ligands to zinc. Reductive reactivation using either DTT or Tris (2-carboxyethyl)phosphine (TCEP) in the presence of Zn^{2+} has been demonstrated for BHMT [16], for the methyltransferase, MT2-A, that methylates coenzyme M [25], and for MetH (Manning and Matthews, personal communication). It is not clear whether this redox behav-

[4]Correspondence: mlludwig@umich.edu

Key words: homocysteine; zinc; methyltransfer; $(\beta/\alpha)_8$ barrel; thiolate ligands; signature sequences

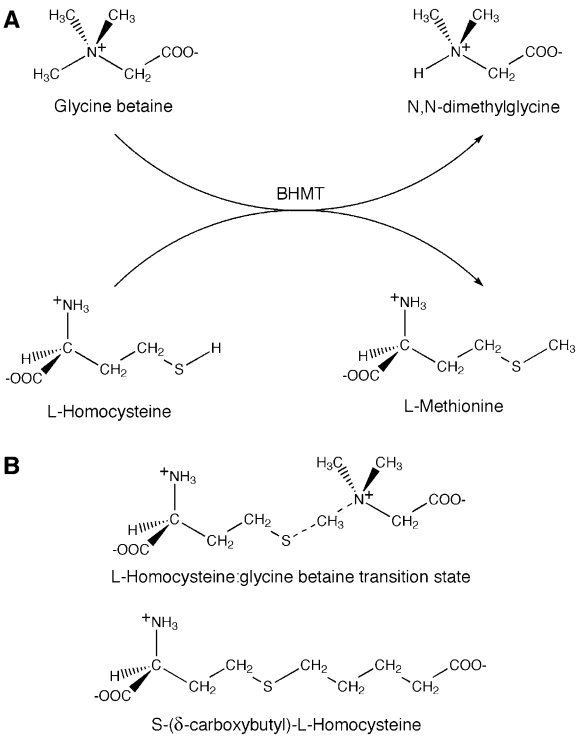

Figure 1. The Reaction Catalyzed by BHMT and a Proposed Transition State

(A) The reaction catalyzed by betaine-homocysteine methyltransferase.

(B) Structure of the transition-state mimic, S(δ-carboxybutyl)-L-homocysteine (CB-Hcy).

ior is a significant mode of physiological regulation, as seems to be the case in the zinc-containing chaperone Hsp33 [26].

We can predict that the fold of BHMT is related to the N-terminal region of B_{12}-dependent methionine synthase, based on sequence similarities of ~40%; there are similar homologies between BHMT and a family of homocysteine methyltransferases from bacterial and plant species [27]. Among the slightly more distant cousins to BHMT are S-methylmethionine thiol/selenol methyltransferases and AdoMet thiol/selenol methyltransferases that can utilize Hcy, Se-Hcy, or Se-cysteine as methyl acceptors [28]. Alignments of some typical family members are shown in Figure 2. MetH is distinguished from the other members by its use of the methylcobalamin cofactor as the methyl donor. All of these methyltransferases are probably dependent on zinc for activity and appear to share mechanistic features [20].

In this paper we describe the structure of BHMT in the oxidized (Zn-free) and reduced (Zn-replete) states. The features and environment of the $Zn(Cys)_3$ sites that are found in BHMT, methionine synthase, and other members of the homocysteine S-methyltransferase family have not previously been determined. The structure of BHMT in complex with the transition-state mimic, S(δ-carboxybutyl)-L-homocysteine, has allowed us to define the interactions that are responsible for substrate binding and specificity.

Results and Discussion

Structure Determination

Structure analyses were carried out with recombinant protein [14] in which the sequence of human liver BHMT had been modified by the substitution of alanine for the five nonessential cysteines at positions 104, 131, 186, 201, and 256 and by the substitution of alanine for proline at position 2 (Figure 2). The enzyme was crystallized by vapor diffusion against 40% PEG 200 and 100 mM sodium citrate (see Experimental Procedures). Crystals formed in space group C2, with cell dimensions of a = 109.5 Å, b = 90.9 Å, c = 89.5 Å, and β = 122.5° and a V_M of 2.07 $Å^3$/Da, corresponding to a dimer in the asymmetric unit.

The structure of a samarium derivative of human BHMT was solved using multiwavelength anomalous dispersion (MAD) measurements at two energies near the L_{III} edge of Sm (Table 1). The very large experimental values of f″ and f′ for this lanthanide ion (Table 1) facilitated the structure determination, especially the initial SAD phasing, which was based on data measured at the peak wavelength (Experimental Procedures). In the samarium derivative the protein was found to be oxidized and Zn free. Model building and refinement at 2.15 Å revealed a disulfide bridge connecting Cys217 and Cys299, two of the three cysteine residues that had been assigned as zinc ligands from mutagenesis experiments [14]. Crystals were reduced with dithiothreitol in the presence of zinc chloride and equilibrated with the transition-state analog, S(δ-carboxybutyl)-L-homocysteine (CB-Hcy). These crystals provided data for a molecular replacement solution of the reduced Zn-replete bisubstrate complex at 2.05 Å resolution (Tables 1 and 2; Experimental Procedures).

In the experimentally phased Sm complex, there are disordered regions at the chain termini and in connections between $(\beta/\alpha)_8$ barrel strands and helices; residues 2–10, 38–52, 76–99, 325–332, and 372–407 are not modeled in this structure. Conversion to the Zn-replete bisubstrate complex resulted in diffraction to higher resolution and maps with interpretable electron density for the loop comprising residues 38–52, which was disordered in the Sm complex. However, we were still unable to model residues 2–10, 83–95, and 372–407. The CB-Hcy complex, refined to an R_{work} of 0.225 (R_{free} of 0.255) and a CC_F of 0.93 [29] for data between 10.0 Å and 2.05 Å, is the more complete structure, and the model of this complex is the basis for our description of the fold and overall features of BHMT.

The Monomer Fold and Dimer Interactions

The principal feature of the fold of BHMT is a $(\beta/\alpha)_8$ barrel formed by residues 11–318 (Figure 3A). The L1 loop between residues 38 and 52 and a long, well-ordered substructure formed by residues 248–276 of the L7 loop lie over the C-terminal ends of the barrel strands. The 38–52 loop, which is ordered in the CB-Hcy complex, seems to play an important role in substrate binding. Beyond residue 318, where the barrel ends, the visible portion of the chain forms an extended substructure that makes intimate interactions with loop L7 of the

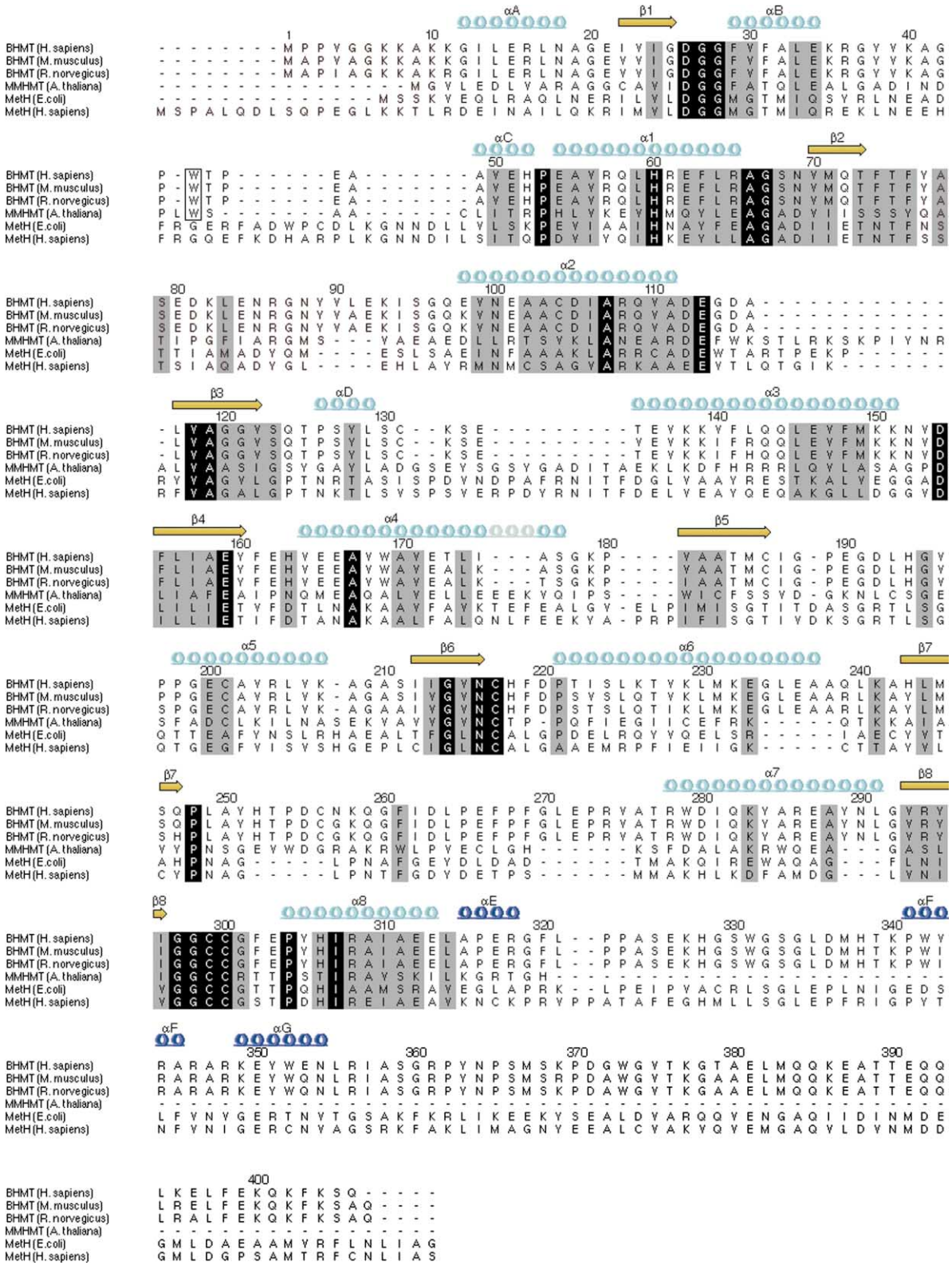

Figure 2. Alignments of Representative Sequences from the Homocysteine S-Methyltransferase Family (Pfam02574)

The N-terminal Met is removed from the recombinant human BHMT (line 1), and the expression construct adds Gly at the C terminus to give a chain of 406 residues. Position 239 is Gln rather than Arg [51]. Alignments were performed with ClustalW [62]. Alignments of additional family members, Cys, Se-Cys, and Se-Hcy methyltransferses, are given elsewhere [28]. MetH is not expected to resemble BHMT beyond residue 350 [21]. The secondary structure of human BHMT is displayed above the sequence alignments. Barrel elements are designated β1–β8 and α1–α8; accessory secondary structures are labeled αA, βA, etc. Sequences 1–10, 83–95, and 372–406 are observed in the electron density for the CB-Hcy complex. Species and accession numbers are: BHMT (*H. sapiens*), Q93088; BHMT (*M. musculus*), NP_057877; BHMT (*R. norvegicus*), NP_110477; MMHMT (*A. thaliana*), AAG10301; MetH (*E. coli*), P13009; MetH (*H. sapiens*), NP_000245.

Table 1. Data Collection

	Native Complex	Sm (Remote)	Sm (Peak)
Resolution (Å)	50–2.05	50–2.15	50–2.15
Highest resolution shell (Å)	2.12–2.05	2.23–2.15	2.23–2.15
Wavelength (Å)	0.90000	1.7462	1.84482
Number of reflections	131,321	148,174	145,650
Number of unique reflections	46,046	40,062	40,209
Completeness (%)[a]	99.8 (100.0)	99.9 (99.9)	98.7 (97.9)
R_{sym}[a,b]	0.057 (0.289)	0.046 (0.213)	0.047 (0.294)
I/σ_I[a]	9.3 (2.5)	17.3 (3.4)	16.0 (2.5)
Redundancy	2.9	3.7	3.6
f′/f″[c]		−10/9.5	−29.0/32.7
Phasing Power[d] (centric/acentric)			4.0/3.0
R_{cullis}[e] (centric/acentric)			0.62/0.66
FOM (before/after DM)			0.60/0.66

[a] Values in parentheses refer to the statistics in the highest resolution shell.
[b] $R_{sym} = \Sigma|I_{obs} - <I>|/\Sigma I_{obs}$.
[c] Experimental values measured for f′ and f″.
[d] Phasing Power = rms ($|F_H|/E$), where $|F_H|$ is the heavy atom structure factor and E is the residual lack of closure error.
[e] $R_{cullis} = \Sigma||F_{H,obs}| - |F_{H,calc}||/\Sigma|F_{H,obs}|$, where $|F_{H,obs}|$ is the observed heavy atom structure factor and $|F_{H,calc}|$ is the calculated heavy atom structure factor.

$(\beta/\alpha)_8$ barrel from the opposite BHMT monomer (Figure 3B). We call this part of the chain the dimerization arm, or motif, since two BHMT monomers are held together in part by the interchain interactions of this structural element. A hook-shaped loop at P^{362}-Y^{363}-N^{364}-P^{365} in the dimerization arm wraps around the equivalent loop in the other monomer (Figures 3B and 4). We surmise that this proline-rich sequence stabilizes the observed intertwining of the two chains. The remaining residues that are visible (366–371) make intrachain contacts. The hook and its neighbors (346–365) are unambiguously defined in omit maps (Figure 4); residues from this part of the arm are well ordered, with average B values of ~31 Å^2.

Formation of the dimer buries approximately 3300 Å^2 of accessible surface [30] (http://www.biochem.ucl.ac.uk/bsm/PP/server). The buried surfaces can be divided into two subregions that differ in composition and area: the interface between the $(\beta/\alpha)_8$ barrels and the interfaces involving the dimerization motifs. The area buried in the interface between the $(\beta/\alpha)_8$ barrels is about 1200 Å^2, with a composition that is 45% hydrophilic and 55% hydrophobic. This interface is thus as polar as exposed surfaces, with 24 interchain hydrogen bonds, including two salt bridges, spanning the gap between the $(\beta/\alpha)_8$ barrels. There are 28 waters trapped in this interface. In contrast, the contacts involving the dimerization motifs are more nonpolar. The interactions that anchor the C-terminal arms to the L7 loops of their dimer partners are specific enough to indicate that these interfaces are not simply artifacts of crystallization. For example, Trp352B tucks into a hydrophobic pocket formed by Pro268A, Phe269A, and Trp279B, and Glu266B hydrogen bonds to the backbone NH of Ala358A. Arginine residues inserted into pockets in the L7 loop substructure form hydrogen bonds with backbone carbonyl oxygens: Arg346A forms a hydrogen bond with Ile262B and Leu264B, and Arg361A forms a hydrogen bond with Pro273B and Val275B. It is likely that these arginine insertions play a significant role in the dimerization of BHMT monomers.

The BHMT Tetramer

The overlap of the hooks formed by P^{362}-Y^{363}-N^{364}-P^{365} provides a flat surface that allows the close approach of another dimer, related by a crystallographic 2-fold axis (Figure 3C). The tetramer interface seen in the crystal is relatively small, burying ~780 Å^2 of accessible surface area, and is predominantly nonpolar in nature (64% hydrophobic) [30]. This is the only dimer-dimer contact in the crystal that can generate a tetramer with 222-point symmetry. Additional tetramer contacts might be made by the disordered sequence following residue 371. However, BHMT in this crystal form is best described as a dimer of dimers, given the extensive dimer interactions and the relatively small tetramer interface.

We are not convinced that the interactions of the dimerization arms are essential for proper folding of the $(\beta/\alpha)_8$ barrel structure shared by members of the homocysteine methyltransferase family. Our expression system used the IMPACT-T7 construct [14, 31], which fuses two separately folded domains to the C terminus for purification purposes. The presence of these additional domains makes it unlikely that the intimate dimer structure forms during folding. It seems more reasonable to suppose that the dimerization is a postfolding event [32]. Comparisons with other members of the homocysteine methyltransferase family also suggest that the C-terminal extension found in BHMT is not necessary for folding. Notably, S-methylmethionine homocysteine methyltransferase, a monomeric protein [27], possesses a shorter sequence, which is predicted to end after α_8 of the $(\beta/\alpha)_8$ barrel (Figure 2). Further, the $(\beta/\alpha)_8$ barrel sequence comprised of residues 2–353 of MetH from *E. coli*, which lacks the C-terminal extension, can be expressed and is able to bind and activate Hcy [21].

BHMT has been presumed to be a hexamer from measurements of elution volumes in gel filtration experiments [13, 17]. Earlier estimates of the aggregate M_r of horse liver BHMT from the sedimentation coefficient suggested a tetramer [9], whereas approach to equilib-

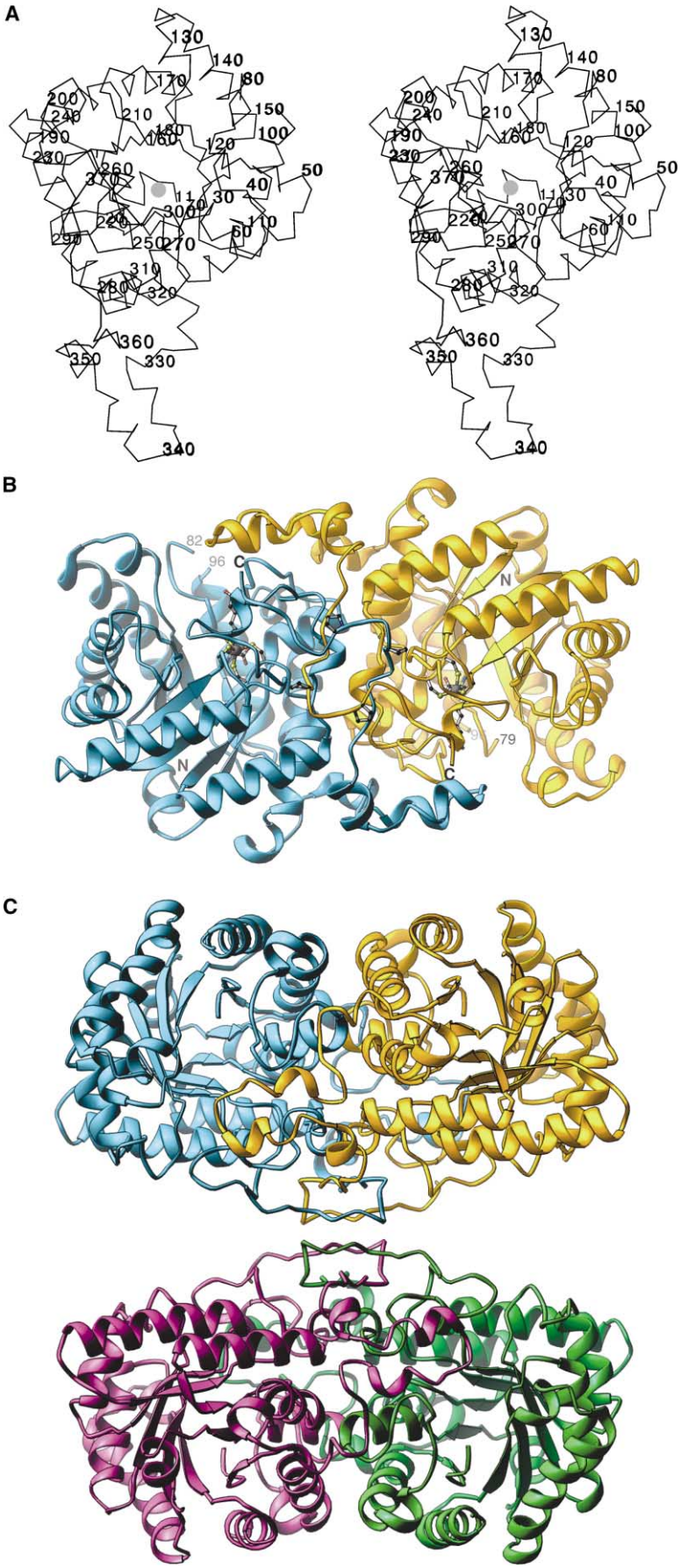

Figure 3. Views of the BHMT Monomer, Dimer, and Tetramer

(A) The BHMT monomer. A stereo view of the Zn-replete enzyme, looking down the axis of the $(\alpha/\beta)_8$ barrel. The Zn ion is the gray sphere. Residues 83–95 in loop L2, which connects $\beta 2$ and $\alpha 2$, are disordered and are not included in the model. The dimerization arm begins at residue 319. This figure was prepared using Swiss-PdbViewer [63].

(B) The BHMT dimer. The two chains that constitute the asymmetric unit are viewed along the local dyad axis and colored to show the interactions of the dimerization arms and the "hooks" at residues P^{362}-Y^{363}-N^{364}-P^{365}. Zn, gray; the transition-state analog and the hook residues Pro362 and Pro365 are represented by ball-and-stick diagrams. This figure and the remaining figures were prepared using RIBBONS [64].

(C) The BHMT tetramer. Coloring distinguishes the four chains that make up the 222 tetramer. The cyan and gold chains comprise the dimer shown in (B), rotated so that the noncrystallographic axis is vertical. The crystallographic dyad is perpendicular to the page and relates the cyan and gold chains to the green and purple chains. The prominent dimer-dimer contacts are made by the hook regions at residues 354–369.

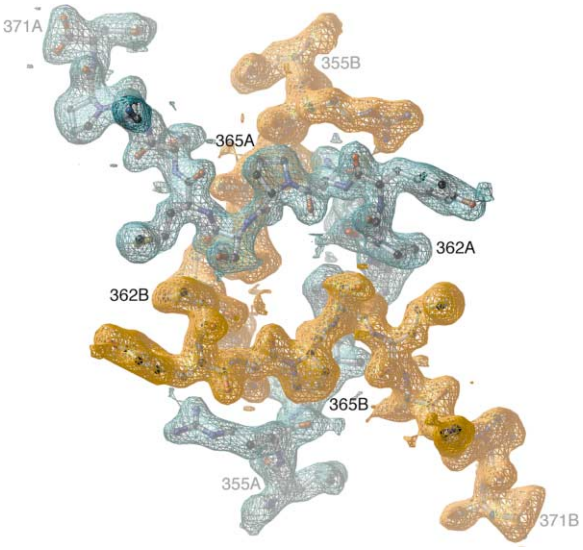

Figure 4. Electron Density at the Hook Region of the Dimer Interface

This view of the final model positioned in a composite simulated-annealing omit map [57] shows the intertwining of the chains and the conformation of the hook sequence P^{362}-Y^{363}-N^{364}-P^{365}. The orientation is the same as in Figure 3B.

rium experiments with the pig liver enzyme were more consistent with a hexamer [11]. Studies of the aggregation states have been complicated by disulfide formation [9, 13]; in fact, the mutations of the five nonessential cysteine residues were performed to prevent irreversible aggregation of the protein at high concentrations. The discrepancies between the sedimentation and gel filtration results make good sense for a particle that is somewhat asymmetric, since the frictional coefficient will make it sediment more slowly but will exclude it more effectively from gels. The flat shape of the crystalline 222 tetramer and presumed flexibility of the C- and N-terminal portions of the chain might therefore account for the measured hydrodynamic properties. But, because the tetramer interface in the crystal is so tenuous, we cannot preclude other modes of aggregation of the dimers in solution.

Barrel Distortion and the Zinc Binding Site

Mutagenesis [14] and sequence alignments [16] have assigned Cys217, Cys299, and Cys300 as the zinc ligands in BHMT. These cysteine residues, located at the C-terminal ends of strands β6 and β8, ligate the catalytic zinc atom in the structure complexed with CB-Hcy. The $(\beta/\alpha)_8$ barrel strands β6 and β8 are pinched together to accommodate the architecture at the zinc site, while strands β1 and β2 are splayed apart near the substrate binding site. These distortions are illustrated in Figure 5. They are generated by the specific conformations and interactions of residues in signature sequences that are conserved in all members of the homocysteine S-methyltransferase family.

To allow close approach of the Cys ligands from strands β6 and β8, which bind the catalytic zinc atom, the intervening strand is extruded from the barrel (Figure 5A). The β7 strand is diverted at the invariant residue Pro248, which is embedded in a conserved sequence [27, 28], suggesting that the kink at β7 is preserved in the entire family of methyltranferases represented in Figure 2. Glycines 297 and 298 from the zinc binding signature sequence enable a tight arrangement of strands β7, β8, and β1 by allowing strand β8 to stretch, permitting the peptide planes along this strand to be oriented perpendicularly to the barrel surface (Figure 5). Thus, the primary roles of the glycine residues in signature sequences [33] are to accommodate close packing at key positions in the distorted barrel.

A cleft is opened where strands β1 and β2 are forced apart by the interaction between Asp26 and the backbone amide of Gln72 from strand β2 (Figure 5B). These strands nevertheless form conventional hydrogen bonding interactions with β8 and β3. An Asp residue is absolutely conserved at the position equivalent to Asp 26 throughout the known homocysteine S-methyltransferase family of proteins and is followed by Gly-Gly or Gly-Ala. The conservation of small amino acids following the invariant Asp residue is important for binding L-homocysteine (below).

Comparison of BHMT with structures in the DALI database [34] revealed that the cleft between strands β1 and β2 (Figure 5B) is similar to a distortion observed in the $(\beta/\alpha)_8$ barrel of uroporphyrin decarboxylase (URO-D) [35]. In both URO-D and BHMT, backbone-backbone interactions between strands β1 and β2 are replaced using side chains from residues near the C-terminal end of strand β1 (Figure 5B). In URO-D, residues 35–38 form a β turn immediately following strand β1, and Gln38 replaces the hydrogen bonds normally found between strands. The opening between strands β1 and β2 in URO-D is thought to be part of the binding cleft for its unusually large substrate, uroporphyrinogen III, and the distortion in this region of BHMT is associated with the binding site for Hcy. Securing strand separation by hydrogen bonding via side chains appears to be a useful device that these functionally unrelated enzymes employ to shape their active sites. Secondary distortions are observed in the BHMT barrel, e.g., partial extrusion of β5, and may be coupled to the major distortions because of the geometric restraints on the folding and packing of $(\beta/\alpha)_8$ barrels [36, 37].

Geometry of the Zinc Site in the Complex with CB-Hcy

Electron density maps of the CB-Hcy complex revealed the zinc atom bound to the sulfur of CB-Hcy and to Cys residues 217, 299, and 300 (Figure 6A). The observation that the alkylated sulfur of the analog CB-Hcy is coordinated to zinc is important in view of discussions about the extent to which the zinc and sulfur are associated during alkyl transfer [38, 39].

For the standard stages of refinement, Zn^{2+} was added to the model and adjusted without any explicit bond length or angle restraints. The resulting ZnS_4 center displayed distorted geometry that was closer to trigonal pyramidal than tetrahedral. The zinc ion and the three S_γ ligands from Cys217, Cys299, and Cys300 were nearly coplanar, with S-Zn-S angles of ~120°, and the sulfur of CB-Hcy was located approximately 2.5 Å above

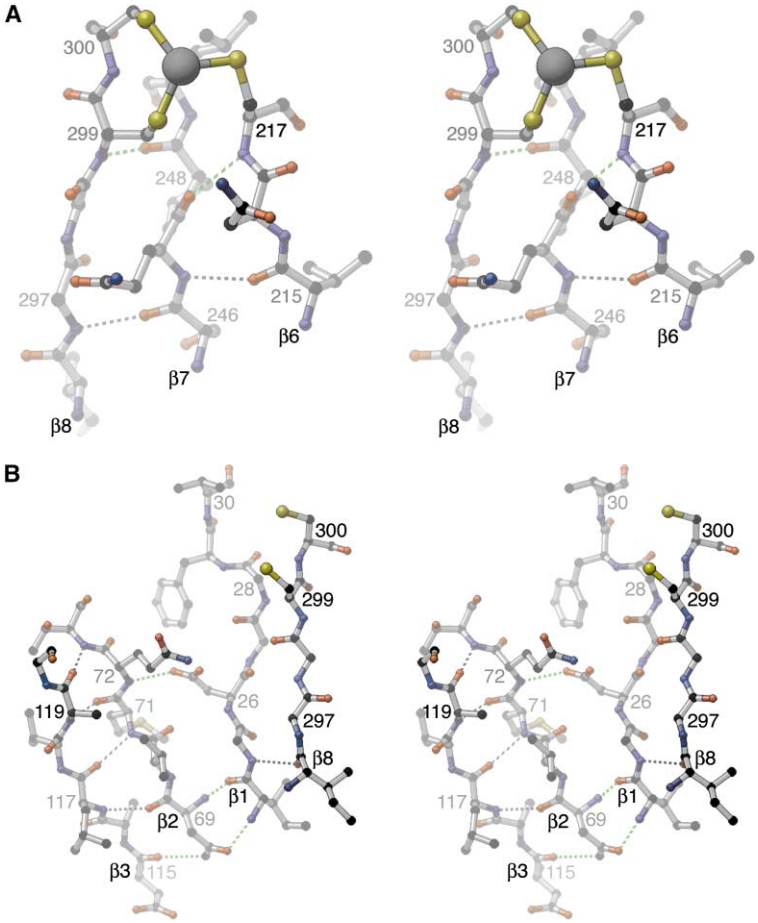

Figure 5. Barrel Conformations and Distortions

(A) A stereo drawing of portions of strands β8, β7, and β6 viewed from inside the BHMT barrel, showing the displacement of strand β7 that allows formation of the $Zn(Cys)_3$ cluster. Starting at Pro248, strand β7 is extruded from the barrel by modest changes in the backbone torsion angles (ϕ and $\Psi = -73°$ and 167° for Pro248). The Cα atoms of Cys217 and Cys299 are separated by only 5.54 Å in the disrupted sheet. Conventional parallel-sheet hydrogen bonds, black; additional hydrogen bonds, green. Cysteines 217 and 299 are part of an irregular top layer of residues whose side chains point toward the interior of the barrel [36].

(B) A stereo view of strands β3, β2, β1, and β8 from inside the barrel. The opening between strands β1 and β2 is secured by Asp26, which hydrogen bonds to NH72. Conventional sheet hydrogen bonds (black) are formed between strand β8 and residues 23 and 25 of strand β1, but there are no conventional hydrogen bonds connecting strands β1 and β2. Strand β1 is displaced toward strand β8 at Gly27 and Gly28. The Hcy binding site and the zinc ligands, Cys299 and Cys300, are at the upper right.

the zinc at an angle of 10° from the normal to the plane of the cysteine sulfurs.

Including tetrahedral restraints on bond lengths and angles during refinement of Cartesian coordinates resulted in a coordination geometry that was closer to tetrahedral, with a negligible increase in R_{work} and R_{free} (<0.004). There were no striking changes in the difference Fourier maps to indicate which geometry is preferred. When the tetrahedral model was subjected to minimization without angle restraints, it relaxed toward the original geometry. The essential difference between the approximately tetrahedral and approximately trigonal pyramidal sites was a displacement of the zinc atom by 0.1 Å, as the sulfur ligands remained in their positions. The current parameters for the zinc site have been taken from a minimization that retained bond length restraints; Zn-S bond lengths vary from 2.26 Å to 2.37 Å, and the angles at Zn range from 99° to 119°. Distortion from tetrahedral geometry might have interesting implications for the reactivity of a bound homocysteine thiolate. Accurate geometries would be helpful in understanding the precise way in which zinc ligation activates the thiolate for nucleophilic attack, as it is not clear how binding to the metal electrophile facilitates this reaction [39, 40]. Unfortunately, our current X-ray data are not sufficiently discriminating to establish the deviations from ideal geometry (Table 2). Structures of protein farnesyltransferase [41, 42] and geranylgeranyltransferase [43], which catalyze analogous zinc-dependent alkyl transfer to a thiolate, are likewise at a resolution too limited to demonstrate distortions.

In metalloproteins the secondary ligand sphere invariably influences the properties of the central metal-ligand cluster. It is interesting that the secondary interactions with cysteine sulfurs in BHMT are much less prominent than those in iron-sulfur clusters or even in the mononuclear sites of Fe- or Zn-rubredoxins [44]. In the CB-Hcy complex, two residues, His218 and Asn216, are likely hydrogen bond donors to Cys217 and Cys299; a well-ordered water interacts with Cys300 (Figure 6B). The interatomic distances are as follows: 216 Nδ–299 S, 3.70 Å; 218 Nδ–217 S, 4.05 Å; WAT O–S 300, 3.33 Å. Of the two protein donors, only Asn216 is invariant among members of the homocysteine methyltransferase family, occurring in the GVNC signature sequence that includes Cys217 in BHMT. The mutation Asn216Ala reduces, but does not eliminate, the catalytic activity of BHMT [14]. Semirandom mutations [33] and known variations at position 218 suggest that potential hydrogen bond donors are favored at this position.

Oxidation of the Active Site

Both BHMT [16] and MetH (Manning and Matthews, personal communication) are susceptible to oxidation and loss of the zinc ion. After inactivation by oxidation or displacement of Zn by modification of the active site

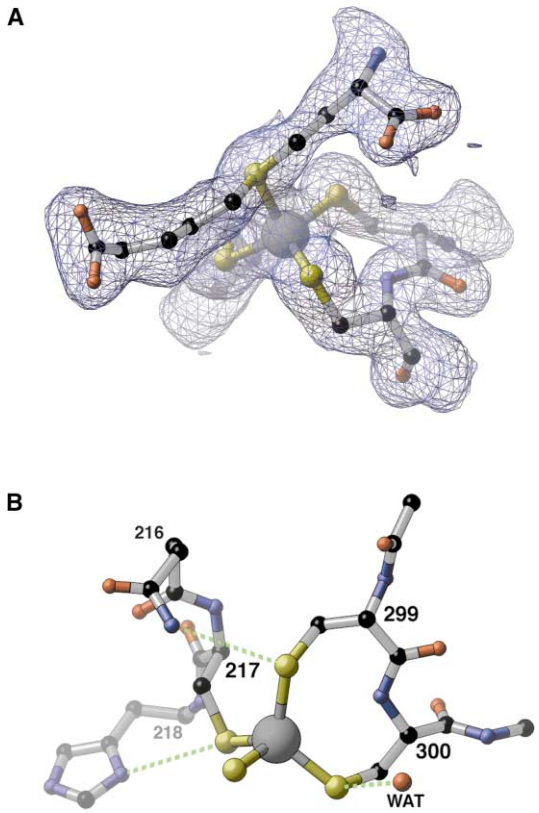

Figure 6. The Zinc Site and Changes Accompanying Oxidation and Loss of Zinc

(A) A simulated-annealing omit map [58] displaying the electron density in the vicinity of zinc in the reduced enzyme.

(B) The geometry of the metal-ligand cluster. Interactions of the cysteine sulfurs with residues 216, 218, and water are indicated with dashed green lines. The water is also hydrogen-bonded to the backbone NH of Phe31. The fourth sulfur is from the bound analog, CB-Hcy.

cysteines with MMTS, BHMT can be reactivated by dialysis versus DTT and Zn^{2+} [16]; related protocols for reactivation after oxidation have been reported for the methyltransferase MT2-A [25]. These methods were adapted for reconstitution of the Zn site in crystalline BHMT (see Experimental Procedures).

It has been assumed that reversible oxidative inactivation entails formation of a disulfide between cysteine residues that serve as zinc ligands. The disulfide is now observed directly in the structure of the Sm derivative of BHMT. Structural changes accompanying oxidation are shown in Figure 7. In the Sm complex, a disulfide bond connects Cys217 and Cys299. Comparison with the reconstituted zinc site shows that the $C\beta$-$S\gamma$ bond of Cys217 rotates $\sim$120° to form the disulfide with $S\gamma$ of Cys299. Formation of the disulfide is accompanied by a flip of the peptide connecting Cys217 and His218, but the conformations of Cys299 and Cys300 are almost identical in the oxidized and reduced structures. In the oxidized enzyme, each of the three active site cysteines adopts a conformation that is only partly allowed, and the rearrangement of Cys217 that occurs on reduction involves a transition from one partly allowed region of the Ramachandran map (ϕ and ψ = 49° and 14°) to a disallowed region (ϕ and Ψ = 65° and −171°).

Table 2. Model Refinement Statistics

	Native Complex	Samarium Derivative
Resolution (Å)	10–2.05	10–2.15
Protein atoms	5340	4824
Waters	428	304
Substrate analog atoms	30	
Zinc atoms	2	
Samarium atoms		4
Citrate atoms	24	24
Average B factor	42.9	36.7
R factor[a]/R_{free}[a]	0.225/0.255	0.203/0.248
Correlation coefficient (CC_F)[b]	0.926	0.923
Rmsd bonds (Å)	0.007	0.018
Rmsd angles (°)	1.426	1.802

[a] R factor = $\Sigma|F_{obs} - F_{calc}|/\Sigma F_{obs}$, where F_{obs} and F_{calc} are the observed and calculated structure factor amplitudes, respectively. R_{free} was calculated using a random set (10%) of the experimental remote data set and a random set (5%) of the native complex data set.

[b] Correlation coefficient calculated using the CCP4 program SFCHECK [29]: $CC_F = (\langle F_{obs}F_{calc}\rangle - \langle F_{obs}\rangle\langle F_{calc}\rangle)/[(\langle F^2_{obs}\rangle - \langle F_{obs}\rangle^2)(\langle F^2_{calc}\rangle - \langle F_{calc}\rangle^2)]^{1/2}$

Oxidation results in disruption of the secondary ligand sphere. Movement of the sulfur of Cys217 and formation of the disulfide break the interaction of Asn216 with the Cys299 sulfur and replace it with a new hydrogen bond to the sulfur of Cys217 (Figure 7B). The ordered water bound to Cys300 is lost in the oxidized enzyme, and the hydrogen bond between Cys217 and His218 is broken. In the zinc-replete enzyme, the secondary interactions may help to stabilize the disallowed conformation of Cys217.

Binding of the Transition-State Analog, S(δ-carboxybutyl)-L-homocysteine

The complex with the transition-state analog was obtained by reducing crystals of oxidized BHMT in the presence of Zn^{2+} and equilibrating with CB-Hcy (see Experimental Procedures). After an initial round of refinement of a model derived from the oxidized Sm complex, electron density maps showed very strong features corresponding to the zinc ion and its sulfur ligands and adjoining density corresponding to bound CB-Hcy (Figure 6A). The final refined occupancy of CB-Hcy is 90% in chain A and 75% in chain B.

The structure of the CB-Hcy complex reveals the interactions that determine the binding of the substrates Hcy and glycine betaine. The sulfur of the transition-state analog is bound directly to the zinc atom, implying that the thiol of Hcy binds zinc, as found from EXAFS measurements on the analogous zinc site in MetH [23]. CB-Hcy also engages in a number of other interactions with the protein, using conserved residues found in members of the homocysteine S-methyltransferase family. The binding site for CB-Hcy can be divided into the two substrate regions, the Hcy subsite that orients L-Hcy in the $(\beta/\alpha)_8$ barrel and a glycine betaine subsite that extends away from the barrel. The L-Hcy site is lined with patches of conserved sequences found in virtually all members of the homocysteine S-methyltransferase

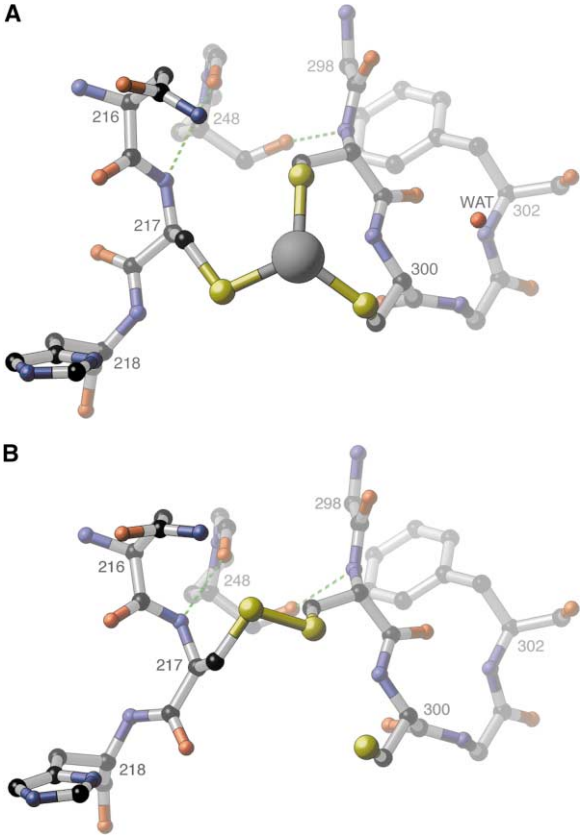

Figure 7. Comparisons of the Zn-Replete Enzyme (A) and the Oxidized Enzyme (B)

Cys217 rearranges to form the disulfide with Cys299; the sulfur of Cys217 moves by rotation about the Cα-Cβ bond, and the 217–218 peptide flips to accommodate formation of the S-S bond.

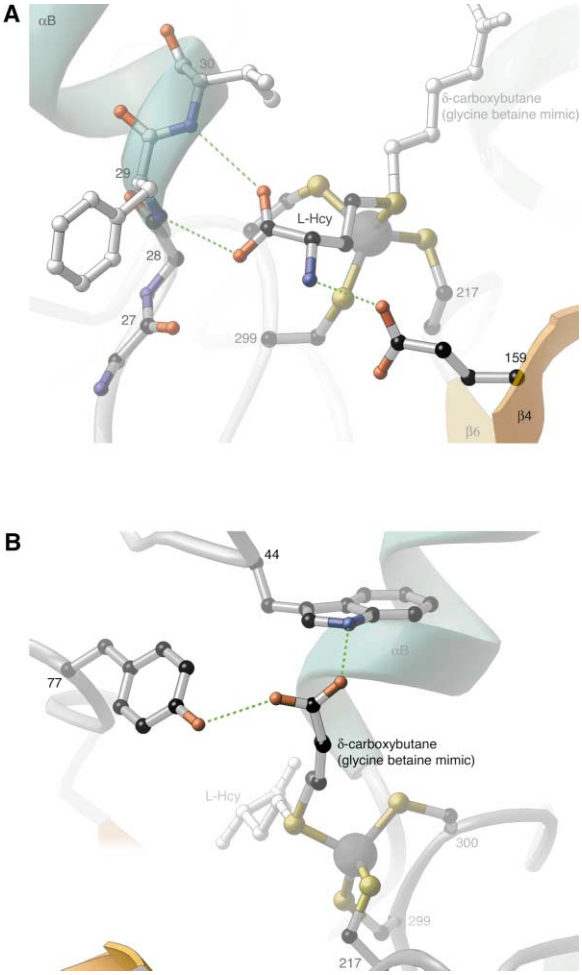

Figure 8. The Interactions of S(δ-Carboxybutyl)-L-Homocysteine (CB-Hcy) with BHMT

(A) A view showing the binding site for L-Hcy and the hydrogen bond interactions that are important for stereospecificity.
(B) A view rotated approximately 90° from (A) showing the interactions of the δ-carboxylate group of CB-Hcy, the analog of the carboxylate of the substrate, glycine betaine.

family, whereas the glycine betaine site is less conserved.

The carboxylate group of the Hcy moiety forms bidentate hydrogen bonds with the backbone amide groups of Phe29 and Val30, located at the start of helix B, a helix in the L1 loop of the barrel (Figure 8A). The fingerprint sequence D^{26}-G^{27}-G/A^{28}, in addition to its role in distorting the barrel, proves to be important in binding the L-Hcy moiety. Small residues at 27 and 28 allow the approach of β1 to β8 (Figure 5B) and, at the same time, permit access of the substrate carboxylate to the backbone at the base of helix B. Because the hydrogen bonding interactions of the L-Hcy are with backbone amides, the residues at positions 29 and 30 do not appear as part of the conserved fingerprint D^{26}-G^{27}-G/A^{28}. BHMT is thus an unusual case in which the residues constituting the sequence fingerprint point indirectly to the sites of substrate interaction.

Glu159 from the C-terminal end of strand β4 reaches across the barrel to hydrogen bond to the amino group of the L-Hcy moiety (Figure 8A). This Glu residue is conserved at a corresponding position in the sequence alignments of the homocysteine S-methyltransferase family. Models of D-Hcy in the active site environment place the amino group more than 4.0 Å away from the carboxylate of Glu 159. Glu 159, therefore, establishes stereospecificity for the L substrate. The shorter Asp is not observed at this position in any of the proteins in the homocysteine S-methyltransferase family. Experimental measurements with the D isomer [15] have shown that it will react and have estimated the stereoselectivity for the L form at high substrate concentrations.

Interactions of the carboxybutyl moiety of CB-Hcy identify the binding site for glycine betaine. The nonpolar butyl chain is surrounded by a series of aromatic residues, including Phe76 and Tyr77 from β2, Tyr160 from β4, and Phe261 and Phe267 from L7. The carboxyl group interacts with Trp44 and Tyr77 (Figure 8B). T.A. Garrow and coworkers (unpublished data) have found a striking increase in intrinsic fluorescence in the presence of both substrates, the CB-Hcy bisubstrate analog, or the appropriate substrate/product pairs (Hcy and DMG). No changes in fluorescence are observed on addition of Hcy, betaine, or DMG alone. The structure of the bisubstrate complex implicates Trp44 as the residue respon-

sible for the fluorescence emission, and the fluorescence data imply that fixing or closure of the loop carrying Trp44 occurs on binding of the second, rather than the first, substrate. Thus, we anticipate that Trp44 will be a convenient probe for detailed analyses of substrate binding and concomitant structural changes.

The Homocysteine S-Methyltransferase Family

Residues 11–320 of BHMT that form the $(\beta/\alpha)_8$ barrel display a high degree of sequence similarity to other members of the homocysteine S-methyltransferase family (Pfam02574), which includes not only the methylmethionine homocysteine methyltransferases and methionine synthases shown in Figure 2, but also the thiol/selenol methyltransferases [28] and the AdoMet homocysteine methyltransferases [27].

Inspection of the interactions between BHMT and CB-Hcy allows us to assign the fingerprint sequences or residues that are signals for substrate binding as D^{26}-G^{27}-G^{28}, Glu^{159}, and Trp^{44}. All of these markers are retained in the enzymes whose substrates are most closely related to those of BHMT. The structure of BHMT and the conservation of the D^{26}-G^{27}-G/A^{28} signature sequence suggest equivalent binding interactions for L-Hcy in all members of the homocysteine S-methyltransferase family. Glu159 is also universally conserved in Pfam02574 and undoubtedly plays a role in both Hcy binding and stereospecificity. However some variations in the nature of the methyl donor are accommodated without losing any of the substrate fingerprints—methylmethionine and even adenosylmethionine are donors for enzymes belonging to Pfam02574 that display all of the substrate markers [27]. AdoMet is not a methyl donor for BHMT [9].

The structure of BHMT establishes Pro248 as an additional marker for the zinc site that had previously been identified by the fingerprints GVNC and GGCC [14, 15, 22]. The conserved Pro248 [27, 28] is important for the architecture of the metal-ligand cluster. Besides diverting β7 away from the barrel core, Pro248 forms a hydrogen bond with the backbone amide of Cys299. A proline at this position thus assists in bringing strands β6 and β8 together to form the Zn binding site (Figure 5A). From the conservation of the three zinc fingerprint sequences and their key positions in the $(\beta/\alpha)_8$ barrel fold, we anticipate that all members of the homocysteine S-methyltransferase family will have the same barrel distortions. In particular, distortions in strands β1 and β7 are predicted for the structure of the N-terminal domain of MetH.

Despite the overall similarities in sequence and in the motifs associated with zinc and Hcy binding, both of which imply homologous folds, BHMT and MetH also differ in characteristic ways. The differences in sequence are most striking in the L1 and L7 loops and are likely to be associated with the evolution of a unique binding site for the very large methyl donor methylcobalamin. L1 carries the marker Trp44, which is involved in binding the methyl donors in BHMT. Although Trp44 is conserved in BHMT, S-methylmethionine homocysteine S-methyltransferase (MMHMT), and the cysteine/selenocysteine methyltransferases, it is not present in MetH. We can predict that the L1 loop of MetH will be 13 residues longer than the corresponding loop in BHMT, based on the alignments of Figure 2. In contrast, the sequence between Pro248 and Cys299, which includes L7, is shortened by 14 residues in MetH. In BHMT the L7 loop forms a substructure that lies over the C terminus of the barrel strands β6, β7, and β8 and is involved in dimerization. Deletion of much of this region in MetH may afford access of methylcobalamin to the Zn-Hcy center.

Biological Implications

BHMT is one of the central enzymes in the pathways for methyl transfer and one-carbon metabolism and is important for homocysteine homeostasis. The structure of this enzyme provides a model for proteins of the homocysteine S-methyltransferase family and defines several prominent features involved in Hcy binding and activation that are undoubtedly applicable to all members of the Pfam02574 set of enzymes involved in alkyl transfer to thiols. All of these enzymes use a catalytic zinc atom bound to highly conserved sequences of residues near the active site, and all are expected to have the same $(\beta/\alpha)_8$ barrel distortions that we have observed in BHMT.

The structure of BHMT and its resemblance to URO-D connect Pfam02574 to other families of structures. Harms and Thauer [45] have detected sequence similarities and fingerprints that relate URO-D (HemE in *E. coli*) to the MT2-A and MT2-M methylcobamide methyltransferases (a.k.a. MtaA and MtbA) that methylate coenzyme M in *Methanosarcina barkeri* [45-47]. Comparison of their alignments and Figure 2 suggests that the G-C-G element of the zinc binding site of MT2-A corresponds to the G-C-C of β8 in BHMT. This connection via URO-D, which is not a zinc-dependent enzyme, would extend the homologies of BHMT beyond the subclass of enzymes that has three cysteine ligands to Zn. There are no three-dimensional structures for MT2-A methyltransferase, but the protein ligands to zinc are two cysteines and one histidine [25].

Other zinc proteins that catalyze alkyl transfer reactions to thiols are known to adopt folds unrelated to BHMT. Included among these are Ada protein [48–50], protein farnesyltransferase [41, 42], and geranylgeranyltransferase [43]. Structures for Ada protein, in which Zn is ligated to four cysteines, reveal the Cys ligands in loops at the ends of adjoining parallel strands. In protein farnesyltransferase and geranylgeranyltransferase, two of the metal ligands, Asp and Cys, are accommodated near the N terminus of a helix from an α-α barrel; the His ligand is from another helix. Comparisons of the reactivities of the homocysteine methyltransferase family with these more diverse proteins [40] will be important in addressing the mechanisms of Zn catalysis and how they vary with the ligand sets or the protein environment.

The structure of BHMT suggests new ways to study the reaction catalyzed by BHMT. Trp44 or other probes can be used to examine the sequence of steps in catalysis, the interdependence of substrate affinities, and the roles of structural changes, particularly the changes in L1 that are inferred from the present structures. Al-

though polymorphisms [51] or other mutations affecting Hcy homeostasis have not yet been targeted to BHMT, the structure offers a rich base of information for interpretation and design of mutations.

Finally, BHMT may offer a structural paradigm for the redox cycling of other $Zn(Cys)_3$ or $Zn(Cys_2His)$ sites. In BHMT, inactivation by disulfide formation and loss of zinc is accompanied by relatively subtle local structural rearrangements and is reversed by reduction in the presence of zinc. Similar inactivation and reactivation has been observed in cobalamin-independent methionine synthases (Manning and Matthews, personal communication) and in the methyltransferase MT2-A [25]; in the latter two enzymes, the ligand sets are Cys_2His, and the cysteine residues are not vicinal. It is unclear whether oxidation is physiologically relevant or merely adventitious in the homocysteine methyltransferase family of enzymes, but zinc thiolate sites do serve as redox response elements in other systems, such as Hsp33 [26].

Experimental Procedures

Crystallization of *Homo sapiens* BHMT

BHMT (5 cys → ala) was expressed as an intein/chitin binding fusion [31] and purified as described previously [14]. The protein was concentrated by ultrafiltration (Amicon-Centricon) to 20 mg/ml in 20 mM Tris (pH 8.0) and 5 mM β-mercaptoethanol. A 1.0 M stock solution of N,N-dimethylglycine (DMG) was added to the protein stock to a final concentration of 10 mM DMG. Equal volumes of the protein/DMG solution and 40% PEG 200 with 0.1 M sodium citrate (pH 5.20) were mixed in Eppendorf tubes (final pH 6.0) and centrifuged to remove precipitate. Eight microliter aliquots of the supernatant in sitting drops were equilibrated at 22°C versus 1.0 ml reservoirs of 40% PEG 200 and 0.1 M sodium citrate (pH 5.20). Clusters of crystals formed after 3 days and grew to a maximum leaflet size of ~50 × 100 × 150 μm after two weeks. These crystals, which contain oxidized, zinc-free enzyme, were harvested and placed in a droplet of artificial mother liquor under Paratone-N immersion oil. Individual single crystals were separated from clusters using a nylon mounting loop. The artificial mother liquor was wicked away from the crystals, and they were flash-cooled in liquid nitrogen. Diffraction analysis determined that the space group was C2, with cell dimensions of a = 109.5 Å, b = 90.1 Å, c = 89.5 Å, and β = 122.5° and two chains in the asymmetric unit, corresponding to a V_M of 2.07. Although several positions beyond residue 371 of BHMT are protease sensitive (J.C.E., unpublished data), gel electrophoresis of protein from the crystals indicated that the polypeptide was the same length as the freshly purified material used for crystallization.

Data Collection for Anomalous Phasing

Crystals were soaked in artificial mother liquor containing 50% saturated samarium (III) acetate for 1 week. After a brief backsoaking in artificial mother liquor, the crystals were transferred to Paratone-N and flash-cooled. Single-wavelength anomalous diffraction (SAD) data at the L_{III} peak of samarium (1.845 Å) were collected at station 17-ID, IMCA-CAT, at the Advanced Photon Source, Argonne National Laboratory. Our original strategy had been to collect MAD data near the L_{III} Sm edge, but radiation damage at these energies precluded collection of the multiwavelength data. Data collected at the peak were used for SAD phasing and yielded a partial model of the structure. Anomalous diffraction data at the peak (1.845 Å) and remote (1.746 Å) wavelengths were subsequently collected at station 5-ID-D, DND-CAT, with a modified strategy that optimized the measurement of anomalous and dispersive differences. Data were processed and scaled using HKL2000, DENZO, and SCALEPACK [52].

Structure Solution

Experimental phases were initially determined from the peak data using SOLVE [53] and later with peak and remote data using both SOLVE and SHARP [54], with four Sm sites per asymmetric unit. The experimental f′ and f″ values, obtained from fluorescence scans, are significantly enhanced by white line effects (Table 1), as observed in other lanthanide derivatives [55, 56]. Density modification in RESOLVE [57] yielded phases with a figure of merit of 0.66 and maps in which most of the structure from residues Lys11–Pro323 was visible in the electron density. An initial model of the $(\beta/\alpha)_8$ barrel was built using XtalView version 4.0 [58]. Two internal loops, 76–100 and 39–51, and several other segments of the sequence were not visible in these initial electron density maps. This initial model was refined in CNS [59] with a maximum-likelihood target using torsional simulated annealing at 5000 K and slow cooling followed by least squares minimization. Phases calculated from this model were combined with the experimental phases, and the resulting σ_A-weighted ($2m|F_o| - D|F_c|$) and ($m|F_o| - D|F_c|$) maps [60] showed very strong density for residues 332–371 at the dimer interface (Figure 4). The inclusion of these fragments decreased the free R factor from 0.43 to 0.39. The final model was developed by rounds of rebuilding and refinement in CNS using data from the remote wavelength to 2.15 Å. Friedel pairs were kept separate throughout refinement to allow for the significant anomalous scattering of samarium. Density corresponding to residues 39–51, 76–100, 323–332, and 371–406 failed to appear in either phase-combined or σ_A-weighted difference maps, and these regions are therefore presumed to be disordered in the oxidized samarium complex. Following several rounds of simulated annealing and least-squares minimization, waters were gradually added to the model at positions with difference densities >2.5 σ if they had acceptable interactions with protein atoms or with other solvents. After the final round of crossvalidated structure refinement, the R_{work}/R_{free} was 0.203/0.248. To examine the models, composite simulating-annealing omit maps were computed at several stages during the refinement of the Sm complex and the CB-Hcy complex (below).

Reduction, Zn Reconstitution, and Ligand Binding

Crystals of oxidized BHMT (5 cys → ala) in artificial mother liquor were transferred to 15 μl dialysis buttons and dialyzed in sealed anaerobic vessels versus 10 ml of 40% PEG 200, 0.1 M citrate (pH 5.20), 10 mM DTT, and 500 μM $ZnCl_2$. The CB-Hcy ligand was included at a concentration of 30 μM. Zinc reconstitution and reduction solutions were purged of oxygen under argon gas for 30 min. Tests of reductants indicated that DTT was preferable to mercaptoethanol or TCEP for reconstitution of the metal site in preformed crystals. After dialysis for 24 hr at 295 K, the crystals were harvested, cryoprotected in Paratone-N, and flash-cooled under liquid nitrogen.

Analysis of Reduced, Zn-Replete BHMT Complexed with CBHcy

Diffraction data from reduced crystals containing Zn and CB-Hcy were collected at station 14-BM-C, BioCARS, APS. Rigid-body refinement of the model of oxidized BHMT, with residues 355–371 omitted, was performed in CNS. The model was then subjected to a round of simulated annealing at 5000 K, with slow cooling in 50° steps, followed by least squares minimization; at this point, R_{work} was 0.342 and R_{free} was 0.398. The σ_A-weighted $2m|F_o| - D|F_c|$ and $m|F_o| - D|F_c|$ maps [58] showed a large positive peak corresponding to the bound zinc atom, as well as clearly interpretable density for CB-Hcy and the loop formed by residues 38–52. CNS parameter and topology files for both stereoisomers of CB-Hcy were generated using the PRO-DRG server [61]. Structure refinement and adjustment of the model followed the protocols described for the Sm complex of BHMT. After inclusion of 428 waters and examination of a final composite omit map the model had an R_{work}/R_{free} of 0.225/0.255 (Table 2).

Acknowledgments

The authors thank Dr. Mark Hilgers for his contributions to the development of this research. The authors are grateful to Dr. Jeanne Stuckey for counsel and assistance with data collection during several trips to APS. Portions of this work were performed at the following experimental stations at the Advanced Photon Source at Argonne, IL: IMCA-CAT 17-ID, DND-CAT 5-ID-D, and BioCARS 14-

BM-C. We are indebted to the staff at IMCA-CAT, DND-CAT, and BioCARS and would particularly like to thank Drs. Andrew Howard, John Quintana, and Keith Brister for their advice and assistance. The facilities of the Industrial Macromolecular Crystallography Association Collaborative Access Team are supported by the companies of the Industrial Macromolecular Crystallography Association through a contract with Illinois Institute of Technology (IIT). The DuPont-Northwestern-Dow Collaborative Access Team Synchrotron Research Center is supported by E.I. DuPont de Nemours and Company, The Dow Chemical Company, the U.S. National Science Foundation (DMR-9304725), and the State of Illinois (1BHE HECA NWU 96). Use of BioCARS Sector 14 was supported by the National Institutes of Health, NCRR (RR07707). Use of the Advanced Photon Source was supported by the U.S. Department of Energy, Basic Energy Sciences, Office of Science, under contract number W-31-102-Eng-38. This research was supported by NIH grants GM16429 (MLL) and DK52501 (TAG) and the Grant Agency of the Czech Republic (B4055003).

Received: April 17, 2002
Revised: May 28, 2002
Accepted: May 30, 2002

References

1. Finkelstein, J.D., and Martin, J.J. (1984). Methionine metabolism in mammals. Distribution of homocysteine between competing pathways. J. Biol. Chem. *259*, 9508–9513.
2. Mosharov, E., Cranford, M.R., and Banerjee, R. (2000). The quantitatively important relationship between homocysteine metabolism and glutathione synthesis by the transsulfuration pathway and its regulation by redox changes. Biochemistry *39*, 13005–13011.
3. Wilken, D.E.L., and Wilken, B. (2001). Historical overview and recent perspectives. In Homocysteine in Health and Disease, R. Carmel and D.W. Jacobsen, eds. (Cambridge: Cambridge University Press) pp. 1–8.
4. Clarke, R., Daly, L., Robinson, K., Naughten, E., Cahalane, S., Fowler, B., and Graham, I. (1991). Hyperhomocysteinemia: An independent risk factor for vascular disease. N. Engl. J. Med. *324*, 1149–1155.
5. Graham, I.M., Daly, L.E., Refsum, H.M., Robinson, K., Brattstrom, L.E., Ueland, P.M., Palma-Reis, R.J., Boers, G.H., Sheahan, R.G., Israelsson, B., et al. (1997). Plasma homocysteine as a risk factor for vascular disease. JAMA *277*, 1775–1781.
6. Refsum, H., Ueland, P.M., Nygard, O., and Vollset, S. (1998). Homocysteine and cardiovascular disease. Annu. Rev. Med. *49*, 31–62.
7. Mizrahi, E.H., Jacobsen, D.W., and Friedland, R.P. (2002). Plasma homocysteine: a new risk factor for Alzheimer's disease? Isr. Med. Assoc. J. *4*, 187–190.
8. Seshadri, S., Beiser, A., Selhub, J., Jacques, P.F., Rosenberg, I.H., D'Agostino, R.B., Wilson, P.W., and Wolf, P.A. (2002). Plasma homocysteine as a risk factor for dementia and Alzheimer's disease. N. Engl. J. Med. *346*, 476–483.
9. Durell, J., Anderson, D.G., and Cantoni, G.L. (1957). The synthesis of methionine by enzymatic transmethylation. Purification and properties of thetin homocysteine methylpherase. Biochim. Biophys. Acta *26*, 270–282.
10. Maw, G.A. (1956). Thetin-homocysteine transmethylase. A preliminary manometric study of the enzyme from rat liver. Biochem. J. *63*, 116–124.
11. Ericson, L.-E. (1960). Betaine-homocysteine-methyl-transferases II. Isolation and properties of the transferase of pig liver. Acta Chem. Scand. *14*, 2113–2126.
12. Fromm, H.J., and Nordlie, R.C. (1959). On the purification and kinetic of rat liver thetin-homocysteine transmethylase. Arch. Biochem. Biophys. *81*, 363–376.
13. Skiba, W.E., Taylor, M.P., Wells, M.S., Mangum, J.H., and Awad, W.M.J. (1982). Human hepatic methionine biosynthesis. Purification and characterization of betaine:homocysteine S-methyltransferase. J. Biol. Chem. *257*, 14944–14948.
14. Breksa, A.P., III, and Garrow, T.A. (1999). Recombinant human liver betaine-homocysteine S-methyltransferase: identification of three cysteine residues critical for zinc binding. Biochemistry *38*, 13991–13998.
15. Garrow, T.A. (1996). Purification, kinetic properties, and cDNA cloning of mammalian betaine:homocysteine methyltransferase. J. Biol. Chem. *271*, 22831–22838.
16. Millian, N.S., and Garrow, T.A. (1998). Human betaine-homocysteine methyltransferase is a zinc metalloenzyme. Arch. Biochem. Biophys. *356*, 93–98.
17. Lee, K.-H., Cava, M., Amiri, P., Ottoboni, T., and Lindquist, R.N. (1992). Betaine:homocysteine methyltransferase from rat liver: purification and inhibition by a boronic acid substrate analog. Arch. Biochem. Biophys. *292*, 77–86.
18. Finkelstein, J.D., Harris, B.J., and Kyle, W.E. (1972). Methionine metabolism in mammals: Kinetic study of betaine-homocysteine methyltransferase. Arch. Biochem. Biophys. *153*, 320–324.
19. Awad, W.M.J., Whitney, P.L., Skiba, W.E., Mangum, J.H., and Wells, M.S. (1983). Evidence for direct methyl transfer in betaine: homocysteine S-methyl-transferase. J. Biol. Chem. *258*, 12790–12792.
20. Matthews, R.G., and Goulding, C.W. (1997). Enzyme-catalyzed methyl transfers to thiols: the role of zinc. Curr. Opin. Chem. Biol. *1*, 332–339.
21. Goulding, C.W., Postigo, D., and Matthews, R.G. (1997). Cobalamin-dependent methionine synthase is a modular protein with distinct regions for binding homocysteine, methyltetrahydrofolate, cobalamin, and adenosylmethionine. Biochemistry *36*, 8082–8091.
22. Goulding, C.W., and Matthews, R.G. (1997). Cobalamin-dependent methionine synthase from *Escherichia coli*: Involvement of zinc in homocysteine activation. Biochemistry *36*, 15749–15757.
23. Peariso, K., Goulding, C.W., Huang, S., Matthews, R.G., and Penner-Hahn, J.E. (1998). Characterization of the zinc binding site in methionine synthase enzymes of *Escherichia coli*: the role of zinc in the methylation of homocysteine. J. Am. Chem. Soc. *120*, 8410–8416.
24. Peariso, K., Zhou, Z.S., Smith, A.E., Matthews, R.G., and Penner-Hahn, J.E. (2001). Characterization of the zinc sites in cobalamin-independent and cobalamin-dependent methionine synthase using zinc and selenium x-ray absorption spectroscopy. Biochemistry *40*, 987–993.
25. Gencic, S., LeClerc, G.M., Gorlatova, N., Peariso, K., Penner-Hahn, J.E., and Grahame, D.A. (2001). Zinc-thiolate intermediate in catalysis of methyl group transfer in *Methanosarcina barkeri*. Biochemistry *40*, 13068–13078.
26. Graumann, J., Lilie, H., Tang, X., Tucker, K.A., Hoffmann, J.H., Vijayalakshmi, J., Saper, M., Bardwell, J.C., and Jakob, U. (2001). Activation of the redox-regulated molecular chaperone Hsp33 - a two-step mechanism. Structure *9*, 377–387.
27. Ranocha, P., Bourgis, F., Ziemak, M.J., Rhodes, D., Gage, D.A., and Hanson, A.D. (2000). Characterization and functional expression of cDNAs encoding methionine-sensitive and -insensitive homocysteine S-methyltransferases from *Arabidopsis*. J. Biol. Chem. *275*, 15962–15968.
28. Neuhierl, B., Thanbichler, M., Lottspeich, F., and Böck, A. (1999). A family of S-methylmethionine-dependent thiol/selenol methyltransferases. J. Biol. Chem. *274*, 5407–5414.
29. Vaguine, A.A., Richelle, J., and Wodak, S.J. (1999). SFCHECK: a unified set of procedures for evaluating the quality of macromolecular structure-factor data and their agreement with the atomic model. Acta Crystallogr. D Biol. Crystallogr. *55*, 191–205.
30. Jones, S., and Thornton, J.M. (1997). Analysis of protein-protein interaction sites using patch analysis. J. Mol. Biol. *272*, 121–132.
31. Chong, S., Mersha, F.B., Comb, D.G., Scott, M.E., Landry, D., Vence, L.M., Perler, F.B., Benner, J., Kucera, R.B., Hirvonen, C.A., et al. (1997). Single-column purification of free recombinant proteins using a self-cleavable affinity tag derived from a protein splicing element. Gene *192*, 271–281.
32. Newcomer, M.E. (2002). Protein folding and three-dimensional domain swapping: a strained relationship? Curr. Opin. Struct. Biol. *12*, 48–53.
33. Breksa, A.P., III, and Garrow, T.A. (2002). Random mutagenesis of the zinc-binding motif of betaine-homocysteine methyltrans-

ferase reveals that Gly 214 is essential. Arch. Biochem. Biophys. *399*, 73–80.
34. Holm, L., and Sander, C. (1997). Dali/FSSP classification of three-dimensional protein folds. Nucleic Acids Res. *25*, 231–234.
35. Whitby, F.G., Phillips, J.D., Kushner, J.P., and Hill, C.P. (1998). Crystal structure of human uroporphyrinogen decarboxylase. EMBO J. *17*, 2463–2471.
36. Lesk, A.M., Bränden, C.-I., and Chothia, C. (1989). Structural principles of α/β barrel proteins: the packing of the interior of the sheet. Proteins: Structure. Funct. Genet. *5*, 139–148.
37. Murzin, A.G., Lesk, A.M., and Chothia, C. (1994). Principles determining the structure of β-sheet barrels in proteins. I. A theoretical analysis. J. Mol. Biol. *236*, 1369–1381.
38. Brand, U., Rombach, M., Seebacher, J., and Vahrenkamp, H. (2001). Functional modeling of cobalamin-independent methionine synthase with pyrazolylborate-zinc-thiolate complexes. Inorg. Chem. *40*, 6151–6157.
39. Wilker, J.J., and Lippard, S.J. (1997). Alkyl transfer to methyl thiolates: kinetics, active species identification, and relevance to the DNA methyl phosphtriester repair center of *Escherichia coli* Ada. Inorg. Chem. *36*, 969–978.
40. Fierke, C.A., and Hightower, K.E. (1999). Zinc-catalyzed sulfur alkylation: insights from protein farnesyltransferase. Curr. Opin. Chem. Biol. *3*, 176–181.
41. Park, H., Boduluri, S., Moomaw, J., Casey, P., and Beese, L.S. (1997). Crystal structure of protein farnesyltransferase a 2.25 Å resolution. Science *275*, 1800–1804.
42. Strickland, C.L., Windsor, W.T., Syto, R., Wang, L., Bond, R., Wu, Z., Schwartz, J., Le, H.V., Beese, L.S., and Weber, P.C. (1998). Crystal structure of farnesyl protein transferase complexed with a CaaX peptide and farnesyl diphosphate analog. Biochemistry *37*, 16601–16611.
43. Zhang, H., Seabra, M.C., and Deisenhofer, J. (2000). Crystal structure of Rab geranylgeranyltransferse at 2.0 Å resolution. Structure *8*, 241–251.
44. Dauter, Z., Wilson, K.S., Sieker, L.C., Moulis, J.-M., and Meyer, J. (1996). Zinc- and iron-rubredoxins from *Clostridium pasteurianum* at atomic resolution: A high-precision model of a ZnS_4 coordination unit in a protein. Proc. Natl. Acad. Sci. USA *93*, 8836–8840.
45. Harms, U., and Thauer, R.K. (1996). Methylcobalamin:coenzyme M methyltransferase isoenzymes MtaA and MtbA from *Methanosarcina barkeri*. Cloning, sequencing and differential expression of the encoding genes, and functional overexpression of the *mtaA* gene in *Escherichia coli*. Eur. J. Biochem. *235*, 653–659.
46. LeClerc, G.M., and Grahame, D.A. (1996). Methyl-cobamide:coenzyme M methyltransferase isozymes from *Methanosarcina barkeri*. Physicochemical characerization, cloning, sequence analysis, and heterologous gene expression. J. Biol. Chem. *271*, 18725–18731.
47. Paul, L., and Krzycki, J.A. (1996). Sequence and transcript analysis of a novel *Methanosarcina barkeri* methyltransferase II homolog and its associated corrinoid protein homologous to methionine synthase. J. Bacteriol. *178*, 6599–6607.
48. Lin, Y., Dotsch, V., Wintner, T., Peariso, K., Myers, L.C., Penner-Hahn, J.E., Verdine, G.L., and Wagner, G. (2001). Structural basis for the functional switch of the *E. coli* Ada protein. Biochemistry *40*, 4261–4271.
49. Myers, L.C., Terranova, M.P., Ferentz, A.E., Wagner, G., and Verdine, G.L. (1993). Repair of methylphosphotriesters through a metalloactivated cysteine nucleophile. Science *261*, 1164–1167.
50. Myers, L.C., Cushing, T.D., Wagner, G., and Verdine, G.L. (1994). Metal-coordination sphere in the methylated Ada protein-DNA cocomplex. Chem. Biol. *1*, 91–97.
51. Heil, S.G., Lievers, K.J., Boers, G.H., Verhoef, P., den Heijer, M., Trijbels, F.J., and Blom, H.J. (2000). Betaine-homocysteine methyltransferase (BHMT): genomic sequencing and relevance to hyperhomocysteinemia and vascular disease in humans. Mol. Genet. Metab. *71*, 511–519.
52. Otwinowski, Z., and Minor, W. (1997). Diffraction-data processing for electronic detectors: theory and practice. Methods Enzymol. *276*, 307–325.
53. Terwilliger, T.C., and Berendzen, J. (1999). Automated MAD and MIR structure solution. Acta Crystallogr. D Biol. Crystallogr. *55*, 849–861.
54. de La Fortelle, E., and Bricogne, G. (1997). Maximum-likelihood heavy-atom parameter refinement for multiple isomorphous replacement and MAD diffraction methods. Methods Enzymol. *276*, 472–494.
55. Brodersen, D.E., Etzerodt, M., Madsen, P., Celis, J.E., Thogersen, H.C., Nyborg, J., and Kjeldgaard, M. (1998). EF-hands at atomic resolution: the structure of human psoriasin (S100A7) solved by MAD phasing. Structure *6*, 477–489.
56. Tomchick, D.R., Turner, R.J., Switzer, R.L., and Smith, J.L. (1998). Adaptation of an enzyme to regulatory function: structure of *Bacillus subtilis* PyrR, a pyr RNA-binding attenuation protein and uracil phosphoribosyltransferase. Structure *6*, 337–350.
57. Terwilliger, T.C. (2000). Maximum-likelihood density modification. Acta Crystallogr. D Biol. Crystallogr. *56*, 965–972.
58. McRee, D. (1999). Practical Protein Crystallography. (San Diego, CA: Academic Press).
59. Brunger, A.T., Adams, P.D., Clore, G.M., DeLano, W.L., Gros, P., Grosse-Kunstleve, R.W., Jiang, J.S., Kuszewski, J., Nilges, M., Pannu, N.S., et al. (1998). Crystallography and NMR system: a new software suite for macromolecular structure determination. Acta Crystallogr. D Biol. Crystallogr. *54*, 905–921.
60. Read, R. (1986). Improved Fourier coefficients for maps using phases from partial structures with errors. Acta Crystallogr. A *42*, 140–149.
61. van Aalten, D.M.F., Bywater, R., Findlay, J.B.C., Hendlich, M., Hooft, R.W.W., and Vriend, G. (1996). PRODRG, a program for generating molecular topologies and unique molecular descriptors from coordinates of small molecules. J. Comput. Aided Mol. Des. *10*, 255–262.
62. Thompson, J.D., Higgins, D.G., and Gibson, J.J. (1994). Nucleic Acids Res. *22*, 4673–4680.
63. Guex, N., and Peitsch, M.C. (1997). SWISS MODEL and the Swiss-PdbViewer: An environment for comparative protein modeling. Electrophoresis *18*, 2714–2723.
64. Carson, M. (1997). Ribbons. Methods Enzymol. *277*, 493–505.

Accession Numbers

The coordinates and structure factors have been deposited with the Protein Data Bank under accession codes 1LT7 (oxidized BHMT) and 1LT8 (CB-Hcy complex of BHMT).